J. Fluid Mech. (2014), *vol.* 746, R1, doi:10.1017/jfm.2014.132

JFM RAPIDS
journals.cambridge.org/rapids

Amplitude modulation of all three velocity components in turbulent boundary layers

K. M. Talluru, R. Baidya, N. Hutchins† and I. Marusic

Department of Mechanical Engineering, The University of Melbourne, Melbourne, Victoria 3010, Australia

(Received 18 December 2013; revised 19 February 2014; accepted 5 March 2014; first published online 31 March 2014)

A combination of cross-wire probes with an array of flush-mounted skin-friction sensors are used to study the three-dimensional conditional organisation of large-scale structures in a high-Reynolds-number turbulent boundary layer. Previous studies have documented the amplitude modulation of small-scale motions in response to conditionally averaged large-scale events, but the data are largely restricted to the streamwise component of velocity alone. Here, we report results based on all three components of velocity and find that the small-scale spanwise and wall-normal fluctuations (v and w) and the instantaneous Reynolds shear stress ($-uw$) are modulated in a very similar manner to that previously noted for the streamwise fluctuations (u). The envelope of the small scale fluctuations for all velocity components is well described by the large-scale component of the u fluctuation. These results also confirm the conditional existence of roll modes associated with the very large-scale or 'superstructure' motions.

Key words: turbulent boundary layers, turbulent flows

1. Introduction

In recent years, an understanding has emerged of the influence of large-scale structures on the near-wall small-scale energy in wall-bounded turbulent flows. These influences are categorised as a linear superposition of large-scale energy onto the near wall and also as a modulation of the small-scale fluctuations by the large-scale motions in the outer layer. It is now fairly well accepted that the growth in the near-wall inner-normalised streamwise turbulence intensity with Reynolds number is due to the increased large-scale energy superimposed onto the near-wall cycle. The phenomenon of large-scale structures modulating the amplitude of small-scale energy was originally studied by Brown & Thomas (1977) and Bandyopadhyay & Hussain (1984) and has been recently highlighted in Hutchins & Marusic (2007). Based on this observation, Mathis, Hutchins & Marusic (2009) developed a mathematical tool

† Email address for correspondence: nhu@unimelb.edu.au

to quantify the degree of amplitude modulation (AM) exerted by the large-scale structure onto the near-wall small-scale events. They also observed that the degree of AM increased with increasing Reynolds number. The method of quantifying AM has been critiqued by Schlatter & Örlü (2010*b*), with alternative methods suggested by Bernardini & Pirozzoli (2011) and Mathis, Hutchins & Marusic (2011). However, at sufficient *Re* all produce results that are consistent with the method of Mathis *et al.* (2009). To date, studies of AM have been largely restricted to analysis of the modulation of the streamwise velocity component. The notable exception here is the recent study of Jacobi & McKeon (2013) who studied AM of streamwise and wall-normal velocity components, albeit at low *Re*. For the current work, we extend this view to quantify the AM of all the small-scale velocity components at high *Re*.

2. Details of the experiments

Experiments are carried out in the high-Reynolds-number boundary-layer wind tunnel at the University of Melbourne, full details of which are given in Nickels *et al.* (2005). All measurements reported here are made 20 m downstream of the tripped inlet to the working section. The free-stream velocity is set close to 20 m s^{-1}, with a nominal boundary-layer thickness of 0.36 m (determined from a fit to the composite profile of Chauhan, Nagib & Monkewitz 2009) and friction velocity, $U_\tau = 0.625$ m s^{-1} (determined by matching the logarithmic mean velocity profile to the constants $\kappa = 0.384$ and $A = 4.17$). This yields a friction Reynolds number $Re_\tau = U_\tau \delta/\nu \approx 15\,000$ (where ν is the kinematic viscosity). The experimental parameters are given in table 1, where θ is the momentum thickness, t is the sampling interval and T is the total sample duration. In this paper, x, y and z refer to the streamwise, spanwise and wall-normal directions while u, v and w denote the corresponding fluctuating velocity components. A spanwise array of nine Dantec 55R47 glue-on type wall-shear stress sensors are arranged with the central sensor positioned directly beneath a cross-wire probe that can be traversed in the wall-normal direction. Skin friction sensors are operated in constant temperature mode with an overheat ratio (OHR) of 1.05 using an AA labs AN 1003 anemometer while the cross-wires are operated with an OHR of 1.6 using an in-house developed Melbourne University Constant Temperature Anemometer (MUCTA). The OHR of 1.6 is chosen to minimise thermal cross-talk between the closely spaced sensors in the cross-wire probe. The experimental set-up used here is similar to the configuration used by Hutchins *et al.* (2011), with the addition of traversing cross-wire probes.

2.1. *Cross-wire probes*

These experiments use subminiature in-house cross-wire probes (see Baidya *et al.* 2012, for details). These probes have etched sensors at $\pm 45^\circ$ with length $l = 0.56$ mm, corresponding to $l^+ = 24$ for the current experimental conditions (yielding $l_x^+ = l_y^+ = 17$ for the *uv* probe, and $l_x^+ = l_z^+ = 17$ for the *uw* probe). The sensor separation is Δs_y or $\Delta s_z = 0.2$ mm (for the *uw* or *uv* probes, respectively) which equates to approximately eight viscous units. Full details are given in table 1. Calibration of the cross-wires is performed *in situ* to eliminate the need to relocate the probe between calibration and the boundary-layer measurement. The calibration rig consists of a jet mounted on a two-axis rotary traversing system allowing rotation along the pitch and yaw axes. For the calibration of the *uw* probe, the sensors are located at the axis of rotation and the jet is pitched using a stepper motor about the spanwise axis. Encoders affixed to

Probe Type	Re_τ	Re_θ	U_∞ (m s^{-1})	ν/U_τ (μm)	U_τ (m s^{-1})	δ (m)	θ (m)	t^+	TU_∞/δ	l_x^+	l_y^+ (or l_z^+)	Δs_z^+ (or Δs_y^+)
uw	15 000	37 100	19.0	24.6	0.620	0.369	0.0294	0.496	30 900	17	17	8.5
uv	15 100	38 400	19.5	24.8	0.624	0.373	0.0304	0.50	31 300	17	17	8.5

TABLE 1. Experimental conditions for different cross-wire configurations.

the yaw and pitch axes provide an accurate measurement of the jet angle relative to the probe. At each of 11 flow velocities, the jet is pitched from $-30°$ to $+30°$. The corresponding voltages from sensors one and two (E_1 and E_2) are recorded to build a voltage-to-velocity conversion map. A similar procedure is used to calibrate the *uv* cross-wire probe, except the jet is yawed about its wall-normal axis. Further details of the calibration procedure can be found in Baidya *et al.* (2012).

2.2. *Validation of the cross-wire measurements*

Figure 1(*a*) compares the measured mean and turbulence intensity profiles of u from the *uv* and *uw* probes against previously reported single hot-wire measurements from the same facility and at matched Reynolds number (Hutchins *et al.* 2011). A good collapse is observed with any discrepancy within expected experimental errors. The non-dimensional sensing length (l^+) used in this study is comparable, but not directly equivalent to the study of Hutchins *et al.* (2011) (see Philip *et al.* 2013, for a full treatment of spatial resolution issues for cross-wire probes). For statistics of the fluctuating v and w components, there is no available direct comparison (owing to a dearth of high-Reynolds-number data at comparable spatial resolution). However, in figure 1(*b*) the measurements are compared with lower-Reynolds-number direct numerical simulation (DNS) data at $Re_\tau = 1271$ (Schlatter & Örlü 2010*a*) and $Re_\tau = 1989$ (Sillero, Jimenez & Moser 2013). The data conform to the expected Reynolds number trends (with some deviation for the v component close to the wall as predicted by Philip *et al.* 2013, for this probe geometry). Furthermore, the data show the logarithmic behaviour in the profile of $\overline{v^2}$, as also highlighted by Sillero *et al.* (2013). The solid line in figure 1(*b*) shows the Reynolds shear stress profile as predicted by integrating the streamwise mean momentum equation across the boundary layer. This compares well to the measured Reynolds shear stress $-\overline{uw}$. Traditionally this is an unforgiving quantity to measure, and the agreement here gives us confidence in the overall ability of the probe and calibration procedure to measure the fluctuating u, v and w components accurately.

3. Three-dimensional conditional view

The signals from the spanwise array of skin-friction sensors are used to detect the footprint of the large-scale structures convecting in the log region of the turbulent boundary layer. The three-dimensional structure of these large-scale events can be revealed by computing various conditional quantities from the *uv* and *uw* probes when a reference hot-film sensor from the spanwise array meets a given condition. To isolate only the large-scale signature of the flow, the fluctuating signals from the skin-friction sensors are first filtered using a Gaussian filter of length 1δ (we will refer to this filtered signal as u_{τ_f}). Based on the measured convection velocity (U_c) of the large-scale events, this equates to a low-pass filter at approximately

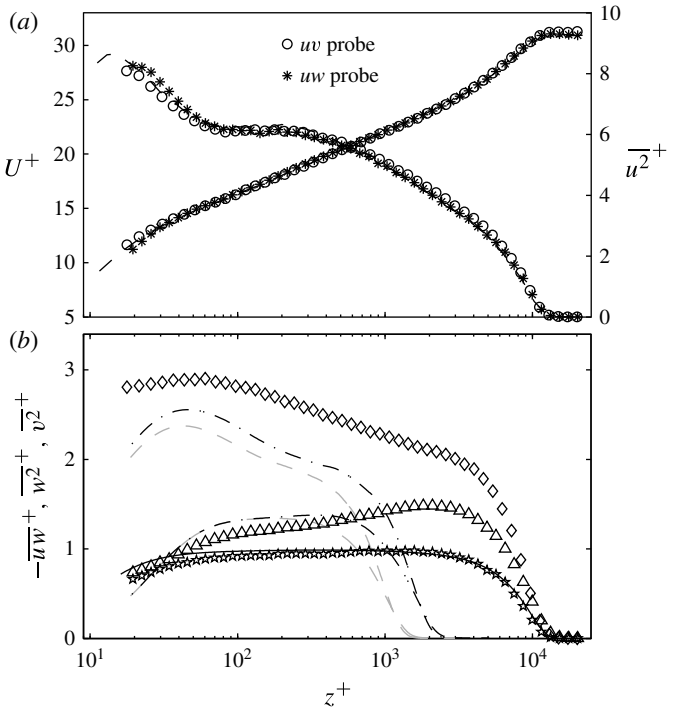

FIGURE 1. (*a*) The mean and variance of the u component as measured by (○) the uv probe and (∗) the uw probe; dashed lines show the data of Hutchins *et al.* (2011) at comparable Reynolds number. (*b*) Comparison of variance of v and w (◊ and △ symbols respectively) against the DNS data of (grey dashed line) Schlatter & Örlü (2010*a*) at $Re_\tau = 1271$ and (dot-dashed line) Sillero *et al.* (2013) at $Re_\tau = 1989$. The measured $-\overline{uw}$ profile (☆) is also compared with the (solid line) Reynolds shear stress obtained from the mean velocity profile.

50 Hz. From such a signal, a large-scale high- or low-skin-friction event is identified when the instantaneous skin-friction fluctuation is greater or less than zero. At those instances when a skin-friction event is detected by a reference skin-friction sensor, the cross-wire measured velocities are conditionally sampled to give an ensemble-averaged velocity signal at a distance Δy and z from the conditioning point, where Δy is the spanwise separation between the cross-wire sensor and the reference skin friction sensor and z is the wall-normal separation between the two. At each of 50 logarithmically spaced stations throughout the wall-normal traverse, the cross-wire signal is conditionally sampled on the occurrence of a low- or high-friction event at each of the nine skin-friction sensors in the spanwise array. This enables reconstruction of a volumetric view of the conditionally averaged event. The conditionally averaged velocity fluctuations based on a negative skin-friction excursion ($u|_l$) can subsequently be defined as

$$u|_l(\Delta t, \Delta y, z) = \langle u(t, y, z) \mid u_{\tau_f}(t - \Delta t, y - \Delta y) < 0 \rangle, \tag{3.1}$$

where u_{τ_f} is the filtered fluctuating friction velocity signal. The time-series hot-wire and hot-film signals are converted using Taylor's hypothesis to a spatial domain ($x = -U_c t$). The convection velocity $U_c = 13.25$ m s^{-1} ($U_c^+ = 21.3$) is determined from

the time-shift in the cross-correlation between two streamwise-separated skin-friction arrays (using a different experimental set-up) and closely matches the mean velocity at the geometric midpoint of the logarithmic region ($z^+ \approx \sqrt{15Re_\tau}$, see Hutchins *et al.* 2011). In (3.1), the streamwise component u can be replaced by a different fluctuating component to calculate the spanwise or wall-normal velocity signature associated with a large-scale skin friction event ($v|_l$ or $w|_l$). To draw a direct comparison with other relevant results reported in the literature, only the low-speed conditional averages are shown here. However, it is noted from our analysis, that the conditional averages based on large-scale high-skin-friction events are nominally the opposite of the conditional averages based on low-skin-friction events.

3.1. *Velocity field associated with a large-scale negative skin friction event*

The isocontours of $u|_l$, $v|_l$ and $w|_l$ are shown in figure 2(*a–c*). Various planes are chosen to highlight the wider three-dimensional structure of a characteristic negative skin friction event centred at $\Delta x = \Delta y = z = 0$. In each of these figures, the x–y plane is drawn at a location $z/\delta \approx 0.002$, the x–z plane is shown at $\Delta y = 0$ (the centreline of the detected large-scale event) and five cross-stream slices in the y–z plane are displayed at locations $\Delta x/\delta = -2, -1, 0, 1, 2$.

Figure 2(*a*) shows the conditionally averaged streamwise velocity depicting an elongated forward-leaning large low-speed feature, extending a distance of $> 5\delta$ in the streamwise direction. This result is consistent with the recent study of Hutchins *et al.* (2011). The spanwise arrangement is more clearly seen in figure 2(*d*), with the low-speed region flanked by high-speed regions on either side. The width of the low-speed region appears to be approximately 0.4δ.

Figure 2(*b*) shows the conditional view of spanwise velocity fluctuations. A nominally zero spanwise fluctuation is observed across the entire centreline plane ($\Delta y = 0$) with elongated regions of opposite signed v on either side of this plane. Close to the wall, figure 2(*b*) indicates that the large-scale low-skin-friction event is accompanied by a spanwise converging motion. Further away from the surface this switches to a diverging motion.

The conditionally averaged map of wall-normal fluctuations is shown in figure 2(*c*). Comparing figure 2(*a*) and (*c*) reveals a strong anticorrelation between u and w events. The large-scale forward leaning low-speed events (that accompany the negative u_{τ_f} fluctuation at the wall) are also characterised by a large-scale region of positive w (flow away from the wall). Thus, low-speed fluid is ejected away from the surface on the centreline of these large-scale events. Flanking this region, we note that high-speed positive u fluctuations from figure 2(*a*) are accompanied by negative w (sweeping of high-speed fluid towards the surface). An important point to notice from figure 2 is that while the u and v components both have a strong large-scale footprint on the x–y plane closest to the wall ($z/\delta \approx 0.002$), the w signature is noticeably weaker (nominally zero) on this plane, indicating a lack of large-scale energy in the w signal close to the wall (due to the impermeability boundary condition).

A closer analysis of the directions of v and w fluctuations in the conditional plots of figure 2(*e*,*f*) reveals the existence of large-scale counter-rotating roll modes. This is best illustrated by plotting the $v|_l$ and $w|_l$ vector field in the planes $\Delta x/\delta = 0$, 1 and 2, as shown in figure 2(*g*). On average, a large-scale structure is located between a pair of large counter-rotating roll modes. In the plane at $\Delta x/\delta = 0$, their spanwise width is $\sim 0.4\delta$ and in the wall-normal direction they extend to 0.4δ from the wall. Streamwise growth of these roll modes is also demonstrated in figure 2(*g*) with the

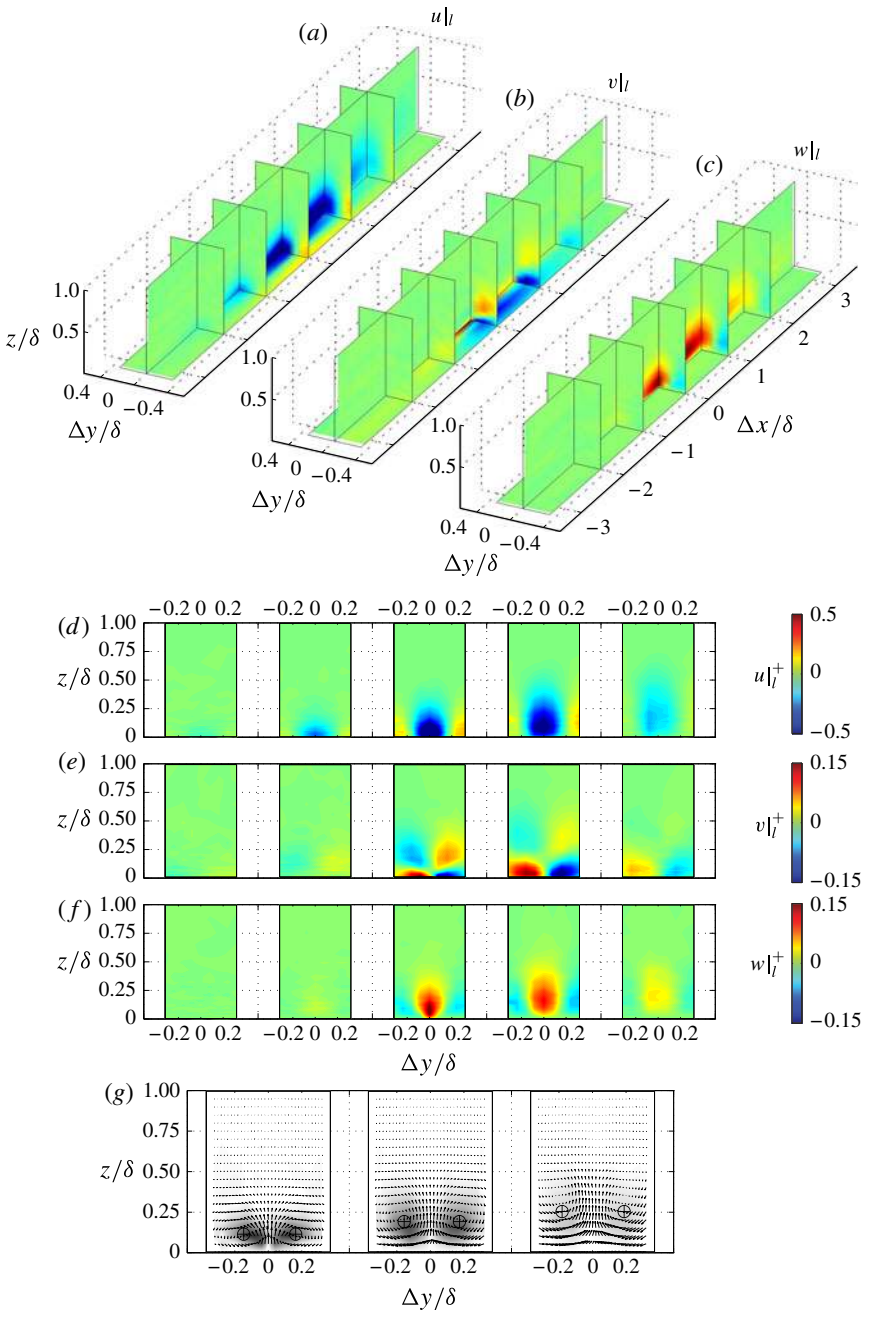

FIGURE 2. Conditional structure associated with a large-scale negative skin friction fluctuation detected at $\Delta x = \Delta y = z \approx 0$. (*a–c*) Isocontours of the fluctuations of $u|_l$, $v|_l$ and $w|_l$, respectively. Three-dimensional view of the x–y plane at $z/\delta = 0.002$, x–z plane at $\Delta y = 0$ and five y–z planes at locations $\Delta x/\delta = -2, -1, 0, 1$ and 2. (*d–f*) Two-dimensional views of y–z planes shown at the five different streamwise locations. (*g*) Roll modes observed in the $v|_l$ and $w|_l$ vector field in the planes, (from left to right) $\Delta x/\delta = 0$, 1 and 2. Grey shaded contours show the absolute streamwise vorticity magnitude. The core locations are marked by the symbol $\oplus$.

three y–z planes illustrating an approximately linear growth in the diameter of these large-scale roll modes with downstream location. The core of these roll modes can be determined through inspection of the maxima in the absolute streamwise vorticity component (grey shaded contours on figure 2*g*). A comparison of the core locations (marked by the symbol $\oplus$) at different Δx planes reveals that they are inclined to the wall at a characteristic angle of approximately 9°.

3.2. *Amplitude modulation of small-scale energy*

A volumetric conditionally averaged view of the small-scale energy in u based on the occurrence of a large-scale low skin-friction event has been shown previously by Hutchins *et al.* (2011). A similar ensemble averaged map of the small-scale variance conditioned on a large-scale negative streamwise fluctuation is given by Bandyopadhyay & Hussain (1984) and by Chung & McKeon (2010). To carry out such an analysis, the signals from the cross-wire probes are filtered using a spectral cut-off filter at $\lambda_x = \delta$, to leave only the small-scale components $u_s = u(\lambda_x < \delta)$. This filter is shown by Hutchins & Marusic (2007) to be effective at separating the inner and outer peaks in the energy spectra of u fluctuations. Filters of length $\lambda_x = \delta$ (Mathis *et al.* 2009; Chung & McKeon 2010; Marusic, Mathis & Hutchins 2010; Mathis *et al.* 2011) and $\lambda_x^+ \approx 7000$ (Hutchins & Marusic 2007; Hutchins *et al.* 2011) have been employed previously in the literature, although Mathis *et al.* (2009) shows that the filter size has very little bearing on the observed modulation. The decomposed small-scale fluctuating signal is subsequently used to analyse how the small-scale variance is modulated by a large-scale low-skin-friction event,

$$\tilde{u}_s^2|_l(\Delta x, \Delta y, z) = \langle u_s^2(x, y, z) \mid u_{\tau_f}(x - \Delta x, y - \Delta y) < 0 \rangle - \overline{u_s^2}, \tag{3.2}$$

where $u_s^2|_l$ is the conditionally averaged small-scale variance associated with a large-scale low-skin-friction event ($u_{\tau_f} < 0$). Note that the tilde notation ($\tilde{u}_s^2|_l$) is used to show the conditionally averaged small-scale variance as compared with the time-averaged unconditional small-scale variance ($\overline{u_s^2}$). A similar conditional analysis is performed on the small-scale signals of v and w fluctuations. It is to be noted that all conditional analyses performed here are based only on the streamwise component of the fluctuating shear stress.

The three-dimensional views of $\tilde{u}_s^2|_l$, $\tilde{v}_s^2|_l$ and $\tilde{w}_s^2|_l$ are shown in figure 3(*a–c*), respectively. The colour scale used in this plot is an indication of the percentage change in the conditioned small-scale variance about the time-averaged unconditional small-scale variance. The amplification of small-scale energy is shown in red shading while the blue shows attenuation. In all of these results, we observe that small-scale energy is attenuated near the wall and amplified farther away from the wall within a low-skin-friction (low momentum) event (the switch from attenuation to amplification occurs at $z^+ \approx 320$ along the line $[\Delta x = \Delta y = 0]$). A similar trend is noted in the conditional average result of Reynolds shear stress shown in figure 3(*d*) which is computed using a conditional scheme similar to that previously explained in (3.2), yet using unfiltered u and w signals:

$$\widetilde{uw}|_l(\Delta x, \Delta y, z) = \langle uw(x, y, z) \mid u_{\tau_f}(x - \Delta x, y - \Delta y) < 0 \rangle - \overline{uw}. \tag{3.3}$$

We also note that the pattern of attenuated and amplified small-scale energy at $\Delta y = 0$ is flanked on both sides (at $\Delta y/\delta \approx \pm 0.4$) by regions of approximately opposite behaviour. This reflects the presence of large-scale conditionally averaged high-momentum events in these locations as shown in figures 2(*a*,*d*). These results are

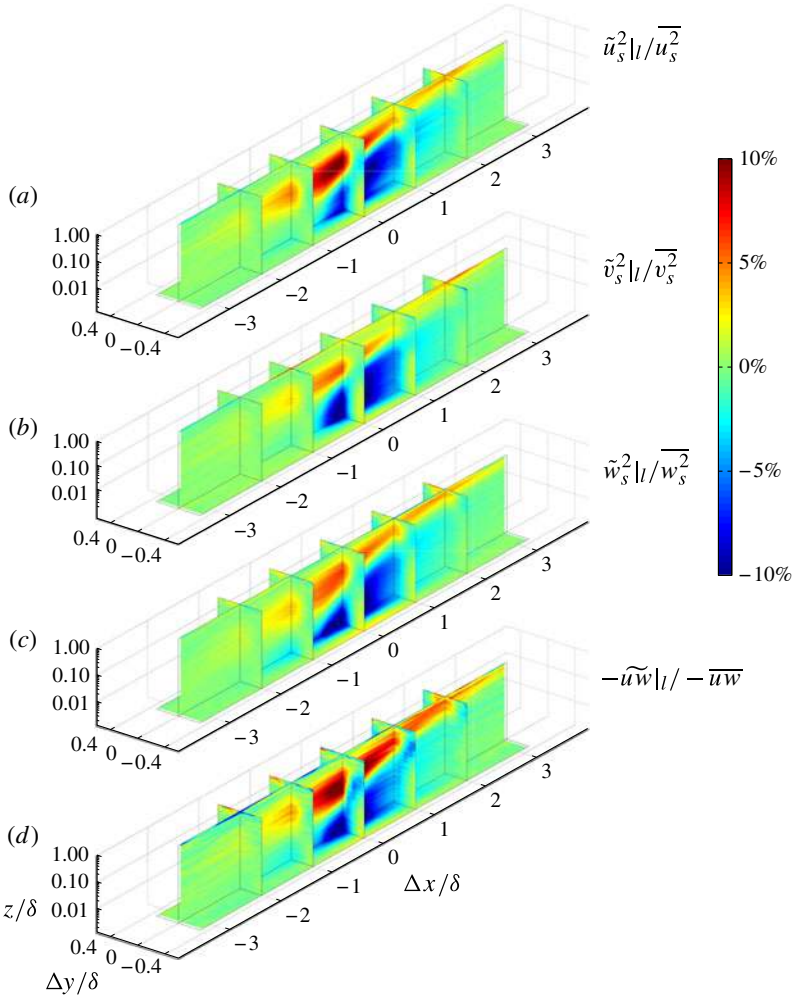

FIGURE 3. Isocontours of percentage change in the small-scale variance of the three velocity components conditionally averaged on a low-skin-friction event: (*a*) streamwise $\tilde{u}_s^2|_l$; (*b*) spanwise $\tilde{v}_s^2|_l$; (*c*) wall-normal $\tilde{w}_s^2|_l$. (*d*) Isocontours of conditional Reynolds shear stress ($-\widetilde{uw}|_l$) as a percentage of mean Reynolds shear stress.

entirely consistent with those shown for the u component by Hutchins *et al.* (2011). However, the surprising and novel result here is that the small-scale u, v, w and unfiltered Reynolds shear stress ($-\overline{uw}$) components are modulated in a very similar fashion about the large-scale conditionally averaged low-skin-friction event. The fact that all components are modulated so consistently about a large-scale streamwise shear-stress event implies that the large-scale streamwise velocity fluctuations measured some distance from the wall may be sufficient to describe the envelope of the small-scale v and w fluctuations. This is explored below in greater detail.

3.3. *Amplitude modulation coefficient*

In the previous section, we have looked at the AM of the small-scale u, v and w based on the large-scale information at the wall. Alternately, one could also look at

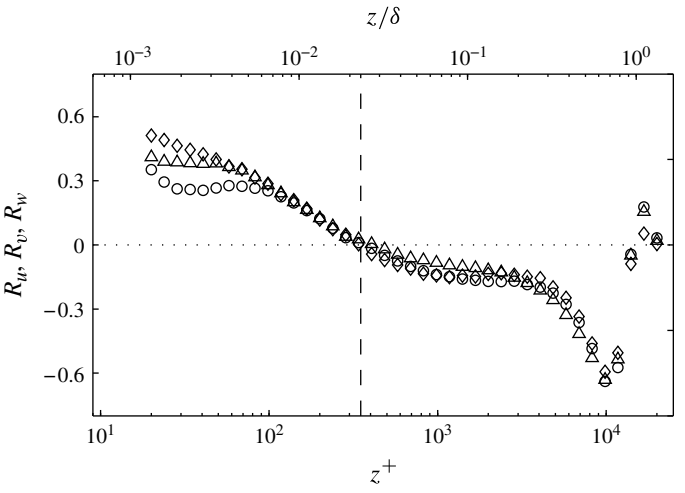

FIGURE 4. AM coefficient for (○) u, (◇) v and (△) w velocity components.

the AM between the large-scale u signal and the small-scale u, v and w at the same given wall-normal location. To do this, we adopt the decoupling procedure given in Mathis *et al.* (2009) to obtain the large-scale component (u_L) and the filtered envelope of the small-scale u fluctuations ($E_L(u_s)$). Using this information, it is then possible to define the (Mathis *et al.* 2009) AM coefficients R_u, R_v and R_w as

$$R_u = \frac{\overline{u_L\ E_L(u_s)}}{\sqrt{\overline{u_L^2}}\sqrt{\overline{E_L(u_s)^2}}}, \quad R_v = \frac{\overline{u_L\ E_L(v_s)}}{\sqrt{\overline{u_L^2}}\sqrt{\overline{E_L(v_s)^2}}}, \quad R_w = \frac{\overline{u_L\ E_L(w_s)}}{\sqrt{\overline{u_L^2}}\sqrt{\overline{E_L(w_s)^2}}}, \qquad (3.4a,b,c)$$

which are essentially the correlation coefficients between the large-scale fluctuations of the streamwise velocity and the filtered envelope of each small-scale velocity component. The results for R_u, R_v and R_w are shown in figure 4 as a function of the wall-normal location. Two observations can be made from the results of R_u, R_v and R_w. First, we note that there is a strong correlation between the large-scale signal (u_L) and the envelope of the small-scale fluctuations u, v and w. The implication here is that the modulation of all three components can be predicted from the streamwise large-scale signal only, measured at a point in the log region of the boundary layer. Second, a similar behaviour is exhibited by all three correlation coefficients. The zero crossings of R_u, R_v and R_w occur at the same wall-normal location in figure 4 (at a location that closely corresponds to the outer peak in the energy spectra of u as noted by Mathis *et al.* 2009). The similar shape of the three profiles seems to suggest that the modulation of the small-scale energy by the large-scale structures is relatively uniform across all three velocity components.

The implications of these results are many, two of which are highlighted here. First, it suggests a possibility to extend the model developed by Marusic *et al.* (2010) to include other velocity components. This model gives a statistically representative streamwise velocity fluctuations at a location z^+ from the wall (u_p^+), the only input being the large-scale streamwise velocity signal from the logarithmic region of the flow (u_{OL}^+). It is expressed as

$$u_p^+(z^+) = u^*(z^+)\overbrace{\{1+\beta_u u_{OL}^+\}}^{\text{modulating component}} + \overbrace{\alpha_u u_{OL}^+}^{\text{superposition component}}, \qquad (3.5)$$

where $u^*(z^+)$ is the statistically universal signal at z^+, and α_u and β_u are, respectively, the superimposition and modulation coefficients (u^*, α_u and β_u are determined from a single calibration experiment). The results presented in figures 3 and 4 suggest that if universal signals for the spanwise and wall-normal components (v^* and w^*) were also determined from a calibration experiment, the model could be extended such that u_{OL} is also used to predict the modulating component of spanwise and wall-normal fluctuations.

The remaining superposition component would require additional work. Figures 2(*d*,*f*) suggest that the large-scale streamwise and wall-normal components are quite anticorrelated, and thus u_{OL} might still provide an appropriate measure of the superposition of w. In the case of spanwise fluctuations, the presence of the roll modes significantly affects the correlation function between the large-scale components of u and v. While the sign of the streamwise fluctuations remains the same along the wall-normal direction, the spanwise fluctuations can change their sign depending on the spanwise location of the input signal within the large-scale event. Thus it is unlikely that a single-point input signal will be adequate to model the superposition component of the spanwise fluctuations.

Another implication of this phenomenon is that it seems to suggest that control schemes targeting large-scale structures could be a viable avenue of future research, since the large-scale superstructure events clearly modulate all three velocity components close to the wall. An example of this is the recent study by Hwang (2013), in which it is shown that the suppression of large-scale features in a turbulent channel flow leads to a reduction of the skin-friction coefficient.

4. Conclusion

The three-dimensional conditional structure of large-scale events in a high-Re turbulent boundary layer has been studied using all three velocity components. It is observed that the large-scale events have a characteristic three-dimensional organisation. A large-scale low-skin-friction event is associated with an elongated forward-leaning low-streamwise-momentum region formed between a counter-rotating roll mode in the conditional v–w velocity fluctuations. It is observed that the small-scale v, w and $-uw$ are modulated in a very similar manner to that previously reported for u, with the envelope of these small-scale fluctuations being well described by the large-scale streamwise fluctuations (u_L). This result opens the possibility of extending the inner–outer interaction model of Marusic *et al.* (2010) to provide predictions of fluctuating v and w (and Reynolds shear stress) signals close to the wall.

Acknowledgements

The authors gratefully acknowledge the Australian Research Council for the financial support of this work.

References

Baidya, R., Philip, J., Hutchins, N., Monty, J. P. & Marusic, I. 2012 Measurements of streamwise and spanwise fluctuating velocity components in a high Reynolds number turbulent boundary layer. In *Proc. 18th Australasian Fluid Mech. Conference*.

Bandyopadhyay, P. R. & Hussain, A. K. M. F. 1984 The coupling between scales in shear flows. *Phys. Fluids* **27** (9), 2221–2228.

BERNARDINI, M. & PIROZZOLI, S. 2011 Inner/outer layer interactions in turbulent boundary layers: a refined measure for the large-scale amplitude modulation mechanism. *Phys. Fluids* **23** (6), 061701.

BROWN, G. L. & THOMAS, A. S. W. 1977 Large structure in a turbulent boundary layer. *Phys. Fluids* **20** (10), S243–S252.

CHAUHAN, K. A., NAGIB, H. M. & MONKEWITZ, P. A. 2009 Criteria for assessing experiments in zero pressure gradient boundary layers. *Fluid Dyn. Res.* **41**, 021404.

CHUNG, D. & MCKEON, B. J. 2010 Large-eddy simulation of large-scale structures in long channel flow. *J. Fluid Mech.* **661**, 341–364.

HUTCHINS, N. & MARUSIC, I. 2007 Large-scale influences in near-wall turbulence. *Phil. Trans. R. Soc.* A **365**, 647–664.

HUTCHINS, N., MONTY, J. P., GANAPATHISUBRAMANI, B., NG, H. C. H. & MARUSIC, I. 2011 Three-dimensional conditional structure of a high-Reynolds-number turbulent boundary layer. *J. Fluid Mech.* **673**, 255–285.

HWANG, Y. 2013 Near-wall turbulent fluctuations in the absence of wide outer motions. *J. Fluid Mech.* **723**, 264–288.

JACOBI, I. & MCKEON, B. J. 2013 Phase relationships between large and small scales in the turbulent boundary layer. *Exp. Fluids* **54** (3), 1–13.

MARUSIC, I., MATHIS, R. & HUTCHINS, N. 2010 Predictive model for wall-bounded turbulent flow. *Science* **329** (5988), 193–196.

MATHIS, R., HUTCHINS, N. & MARUSIC, I. 2009 Large-scale amplitude modulation of the small-scale structures in turbulent boundary layers. *J. Fluid Mech.* **628**, 311–337.

MATHIS, R., HUTCHINS, N. & MARUSIC, I. 2011 A predictive inner–outer model for streamwise turbulence statistics in wall-bounded flows. *J. Fluid Mech.* **681**, 537–566.

NICKELS, T. B., MARUSIC, I., HAFEZ, S. & CHONG, M. S. 2005 Evidence of the k_1^{-1} law in a high-Reynolds-number turbulent boundary layer. *Phys. Rev. Lett.* **95**, 074501.

PHILIP, J., BAIDYA, R., HUTCHINS, N., MONTY, J. P. & MARUSIC, I. 2013 Spatial averaging of streamwise and spanwise velocity measurements in wall-bounded turbulence using v- and x-probes. *Meas. Sci. Technol.* **24**, 115302.

SCHLATTER, P. & ÖRLÜ, R. 2010*a* Assessment of direct numerical simulation data of turbulent boundary layers. *J. Fluid Mech.* **659**, 116–126.

SCHLATTER, P. & ÖRLÜ, R. 2010*b* Quantifying the interaction between large and small scales in wall-bounded turbulent flows: a note of caution. *Phys. Fluids* **22** (5), 051704.

SILLERO, J. A., JIMENEZ, J. & MOSER, R. D. 2013 One-point statistics for turbulent wall-bounded flows at Reynolds numbers up to $\delta^+ = 2000$. *Phys. Fluids* **25** (10), 105102.